Journal of Geophysical Research: Solid Earth

Supporting Information for

Excitation of back-arc tsunamis from megathrust ruptures:

Theory and application to the Sea of Japan

Amir Salaree and Yihe Huang

University of Michigan, Ann Arbor, MI, USA

Contents of this file

Sections S1 to S13
Figures S1 to S15
Equation S1
Tables S1 to S3

Introduction

The supporting information includes 15 figures:

Figure S1 shows the slip distribution of the available finite fault models for the 2011 Tohoku rupture.

Figure S2 includes trench-perpendicular profiles of topography, slip and depth along the transects in Fig. S1.

Figure S3 shows the dominant resonance periods for a 19.5° × 15.5° closed basin.

Figure S4 shows time series for the virtual gauges in Figs. 4 and 5.

Figure S5 illustrates the geometry of how source size and dip can affect surface deformation.

Figure S6 shows longer tide gauge simulations of back-arc waveforms.

Figure S7 shows the back-arc recorded and simulated time series and spectra at Japanese stations.

Figure S8 includes maximum simulated tsunami wave heights from various components of the 2011 Tohoku source.

Figure S9 illustrates the importance of 30-minute time intervals in the calculation of CC between tide gauge records and simulations.

Figure S10 shows relative arrivals of the simulated tsunami into the Korea Strait with respect to Busan.

Figure S11 includes examples of tsunami beamforming near Busan.

Figure S12 visualizes the ray-tracing of the 2011 back-arc tsunami in the Sea of Japan.

Figure S13 shows spectrograms of recorded data at western tide gauges.

Figure S14 compares contribution of near- and far-field components of back-arc deformation to the record from Rudnaya Pristan.

Figure S15 shows a simulation of the 2004 Sumatra tsunami.

Table S1 lists source parameters along with dominant tsunami periods (T_d) and equivalent source dimensions (L_d) from our synthetic simulations.

Table S2 lists the historical sources in the Japan Trench used in constructing the rupture scenarios in this study.

Table S3 lists source properties of the four Nankai Trough rupture scenarios.

S1. Finite Fault Solutions for the 2011 Tohoku Rupture

Fig. S1 shows maps of available finite rupture models for the 2011 Tohoku earthquake in the form of geographic distribution of slip. Trench-perpendicular profiles of topography/bathymetry, slip and depth along the black transects in Fig. S1 are shown in Fig. S2. Fig. S1 and S2 show that the down-dip extent of the rupture is not considered or resolved in the finite fault solutions.
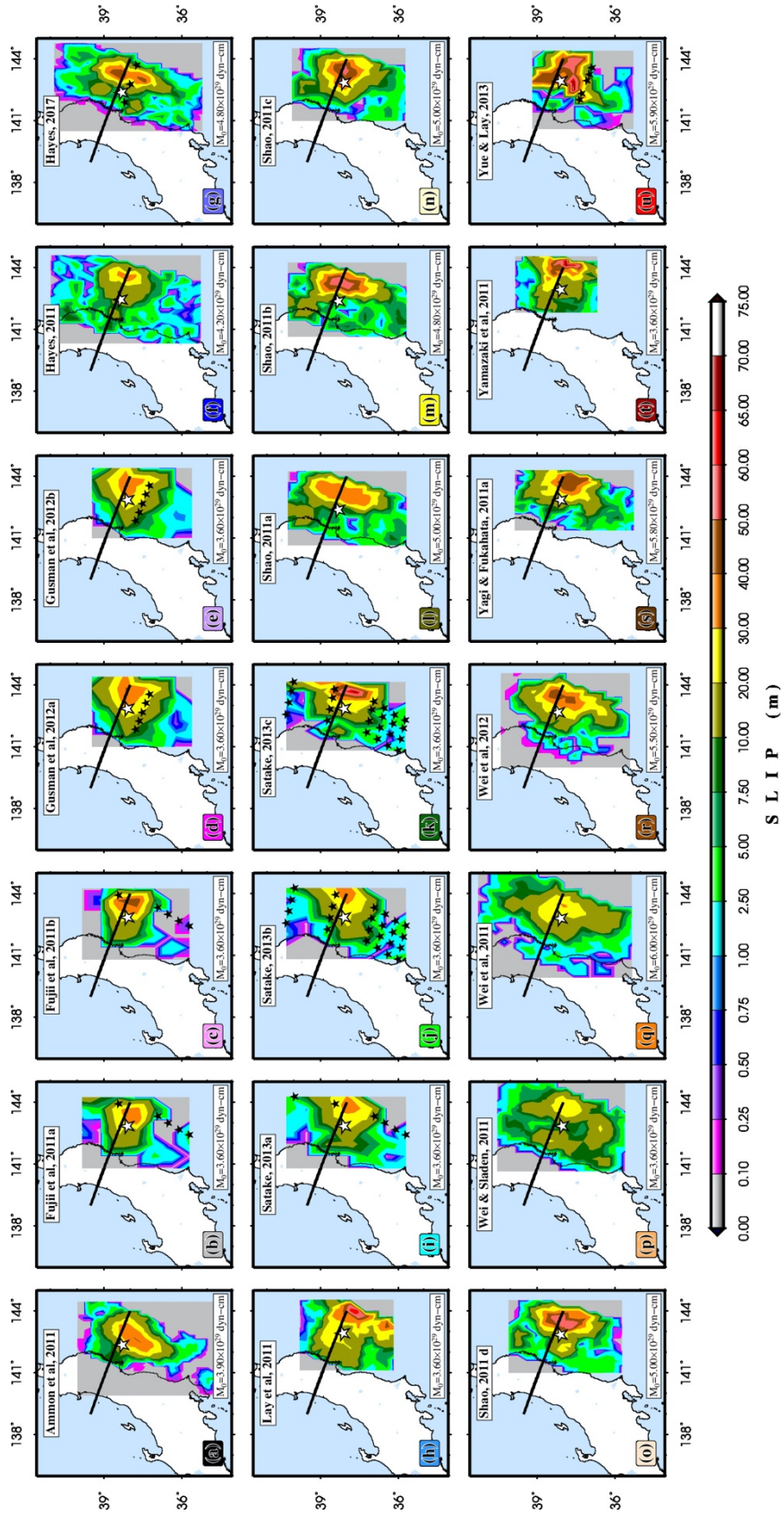
Figure S1. Finite fault models for the for the 2011 Tohoku rupture. Maps are color-coded according to the absolute value of slip (data from SRCMOD; Mai & Thingbaijam [2014]).
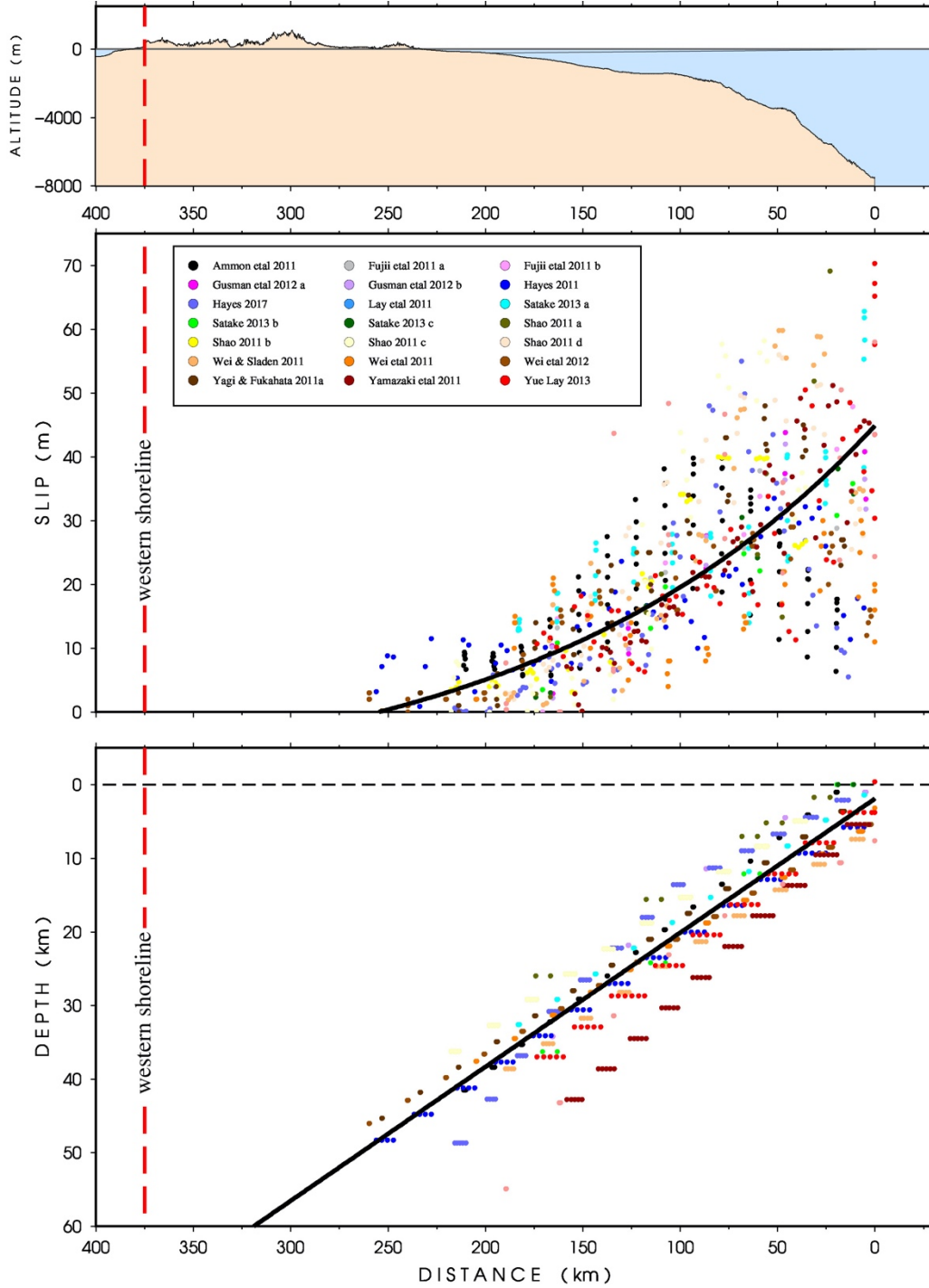
4

Figure S2. (top) Bathymetric and topographic profile of the Japan Trench near Honshu in the direction perpendicular to the trench (black solid lines across Fig. S1); **(middle)** Trench-perpendicular profile of slip from the models in Fig. S1; **(bottom)** Depth profile of the models in Fig. S1 along the same direction as the middle panel.

S2. Resonance modes in closed basins

One can show [Kian, 2015] that free oscillations of tsunamis in a rectangular, closed $a \times b$ basin with the depth of h are given by the formula

$$f = \frac{\sqrt{gh}}{2}\left[\left(\frac{m}{a}\right)^2 + \left(\frac{n}{b}\right)^2\right]^{1/2} \tag{1}$$

where g is acceleration due to gravity and m and n are integers serving as mode multipliers along the a and b dimensions of the basin. Using the first 10 multipliers, we can calculate the dominant periods of free oscillation in a 1000 m deep, 19.5° × 15.5° basin (see section 4.3) as shown in Fig. S3. The hot colors in Fig. S3 belong to higher modes of oscillation, but usually correspond to lower energies and play an insignificant role in the distribution of energy.
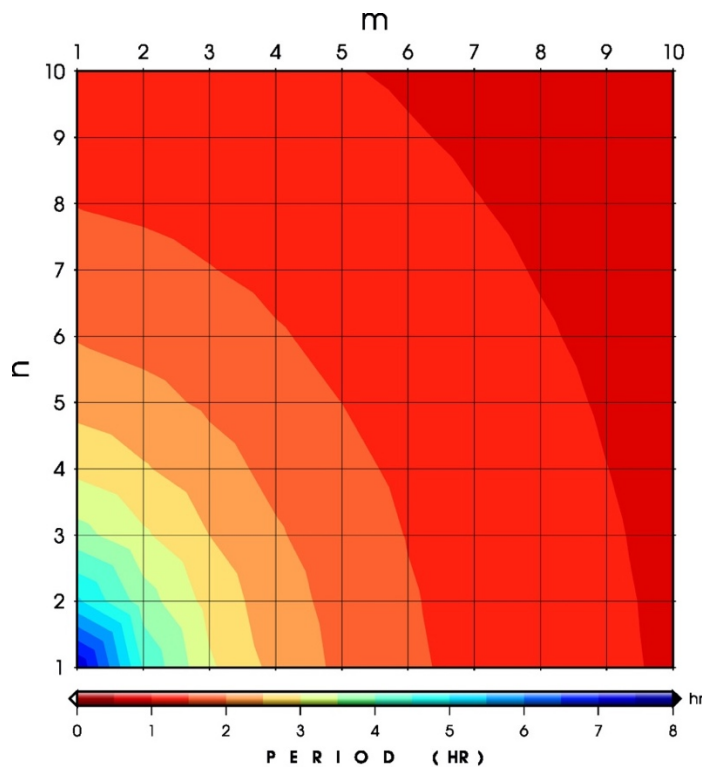

Figure S3. Dominant resonance periods for a 19.5° × 15.5° closed basin.

S3. Results of Synthetic Experiments on Back-arc vs Fore-arc Tsunamis

Table S1 includes source and simulation parameters of both back- and fore-arc tsunamis in each simulation scenario.

Table S1. Source parameters along with dominant tsunami periods (T_d) and equivalent source dimensions (W_e) from our synthetic simulations.

Source Parameters				Back-arc		Fore-arc	
H (km)	M_w	δ	λ	T_d (hr)	L_w (deg.)	T_d (hr)	L_w (deg.)
10	8.0	10	90	3.79	12.29	0.32	2.09
10	8.0	10	75	3.79	12.29	0.32	2.09
10	8.0	10	50	3.79	12.29	0.32	2.08
10	8.0	10	40	3.79	12.29	0.32	2.08
10	8.0	20	90	2.76	8.94	0.33	2.11
10	8.0	20	75	2.76	8.94	0.33	2.11
10	8.0	20	50	2.76	8.94	0.33	2.11
10	8.0	20	40	2.76	8.94	0.33	2.11
10	8.0	30	90	2.76	8.94	0.33	2.15
10	8.0	30	75	2.76	8.94	0.33	2.15
10	8.0	30	50	2.76	8.94	0.33	2.15
10	8.0	30	40	2.76	8.94	0.33	2.15
10	8.0	40	90	2.76	8.94	0.27	1.74
10	8.0	40	75	2.76	8.94	0.27	1.74
10	8.0	40	50	2.76	8.94	0.27	1.74
10	8.0	40	40	2.76	8.94	0.27	1.74
10	8.5	10	90	1.69	5.46	1.62	10.53
10	8.5	10	75	1.69	5.46	1.62	10.53
10	8.5	10	50	1.69	5.46	1.62	10.53
10	8.5	10	40	1.69	5.46	1.62	10.53
10	8.5	20	90	2.76	8.94	1.62	10.53
10	8.5	20	75	2.76	8.94	1.62	10.53
10	8.5	20	50	2.76	8.94	1.62	10.53
10	8.5	20	40	2.76	8.94	1.62	10.53
10	8.5	30	90	5.69	18.43	1.62	10.53
10	8.5	30	75	5.69	18.43	1.62	10.53
10	8.5	30	50	5.69	18.43	1.62	10.53
10	8.5	30	40	5.69	18.43	1.62	10.53

10	8.5	40	90	5.69	18.43	1.66	10.72
10	8.5	40	75	5.69	18.43	1.66	10.72
10	8.5	40	50	5.69	18.43	1.66	10.72
10	8.5	40	40	5.69	18.43	1.66	10.72
10	9.0	10	90	1.42	4.61	2.94	19.03
10	9.0	10	75	1.42	4.61	2.94	19.03
10	9.0	10	50	1.42	4.61	2.94	19.03
10	9.0	10	40	1.42	4.61	2.94	19.03
10	9.0	20	90	1.86	6.02	2.94	19.03
10	9.0	20	75	1.86	6.02	2.94	19.03
10	9.0	20	50	1.86	6.02	2.94	19.03
10	9.0	20	40	1.86	6.02	2.94	19.03
10	9.0	30	90	2.33	7.56	2.94	19.03
10	9.0	30	75	2.33	7.56	2.94	19.03
10	9.0	30	50	2.33	7.56	2.94	19.03
10	9.0	30	40	2.33	7.56	2.94	19.03
10	9.0	40	90	3.64	11.8	2.94	19.03
10	9.0	40	75	3.64	11.8	2.94	19.03
10	9.0	40	50	3.64	11.8	2.94	19.03
10	9.0	40	40	3.64	11.8	2.94	19.03
20	8.0	10	90	2.76	8.94	0.32	2.08
20	8.0	10	75	2.76	8.94	0.32	2.08
20	8.0	10	50	2.76	8.94	0.32	2.08
20	8.0	10	40	2.76	8.94	0.32	2.08
20	8.0	20	90	2.76	8.94	0.33	2.11
20	8.0	20	75	2.76	8.94	0.33	2.11
20	8.0	20	50	2.76	8.94	0.33	2.11
20	8.0	20	40	2.76	8.94	0.33	2.11
20	8.0	30	90	2.76	8.94	0.33	2.15
20	8.0	30	75	2.76	8.94	0.33	2.15
20	8.0	30	50	2.76	8.94	0.33	2.15
20	8.0	30	40	2.76	8.94	0.33	2.15
20	8.0	40	90	5.35	17.35	0.27	1.74
20	8.0	40	75	5.35	17.35	0.27	1.74
20	8.0	40	50	5.35	17.35	0.27	1.74
20	8.0	40	40	5.35	17.35	0.27	1.74
20	8.5	10	90	2.33	7.56	1.60	10.35
20	8.5	10	75	2.33	7.56	1.60	10.35
20	8.5	10	50	2.33	7.56	1.60	10.35

20	8.5	10	40	2.33	7.56	1.60	10.35
20	8.5	20	90	2.76	8.94	1.62	10.53
20	8.5	20	75	2.76	8.94	1.62	10.53
20	8.5	20	50	2.76	8.94	1.62	10.53
20	8.5	20	40	2.76	8.94	1.62	10.53
20	8.5	30	90	5.69	18.43	1.62	10.53
20	8.5	30	75	5.69	18.43	1.62	10.53
20	8.5	30	50	5.69	18.43	1.62	10.53
20	8.5	30	40	5.69	18.43	1.62	10.53
20	8.5	40	90	5.69	18.43	1.66	10.72
20	8.5	40	75	5.69	18.43	1.66	10.72
20	8.5	40	50	5.69	18.43	1.66	10.72
20	8.5	40	40	5.69	18.43	1.66	10.72
20	9.0	10	90	1.6	5.17	2.94	19.03
20	9.0	10	75	1.6	5.17	2.94	19.03
20	9.0	10	50	1.6	5.17	2.94	19.03
20	9.0	10	40	1.6	5.17	2.94	19.03
20	9.0	20	90	1.86	6.02	2.94	19.03
20	9.0	20	75	1.86	6.02	2.94	19.03
20	9.0	20	50	1.86	6.02	2.94	19.03
20	9.0	20	40	1.86	6.02	2.94	19.03
20	9.0	30	90	2.33	7.56	2.94	19.03
20	9.0	30	75	2.33	7.56	2.94	19.03
20	9.0	30	50	2.33	7.56	2.94	19.03
20	9.0	30	40	2.33	7.56	2.94	19.03
20	9.0	40	90	3.64	11.8	2.94	19.03
20	9.0	40	75	3.64	11.8	2.94	19.03
20	9.0	40	50	3.64	11.8	2.94	19.03
20	9.0	40	40	3.64	11.8	2.94	19.03
30	8.0	10	90	2.68	8.67	0.46	2.95
30	8.0	10	75	2.68	8.67	0.46	2.95
30	8.0	10	50	2.68	8.67	0.46	2.95
30	8.0	10	40	2.68	8.67	0.46	2.95
30	8.0	20	90	2.76	8.94	0.32	2.10
30	8.0	20	75	2.76	8.94	0.32	2.10
30	8.0	20	50	2.76	8.94	0.32	2.10
30	8.0	20	40	2.76	8.94	0.32	2.10
30	8.0	30	90	2.76	8.94	0.33	2.15
30	8.0	30	75	2.76	8.94	0.33	2.15

30	8.0	30	50	2.76	8.94	0.33	2.15
30	8.0	30	40	2.76	8.94	0.33	2.15
30	8.0	40	90	5.35	17.35	0.30	1.95
30	8.0	40	75	5.35	17.35	0.30	1.95
30	8.0	40	50	5.35	17.35	0.30	1.95
30	8.0	40	40	5.35	17.35	0.30	1.95
30	8.5	10	90	2.33	7.56	0.45	2.92
30	8.5	10	75	2.33	7.56	0.45	2.92
30	8.5	10	50	2.33	7.56	0.45	2.92
30	8.5	10	40	2.33	7.56	0.45	2.92
30	8.5	20	90	2.76	8.94	1.62	10.53
30	8.5	20	75	2.76	8.94	1.62	10.53
30	8.5	20	50	2.76	8.94	1.62	10.53
30	8.5	20	40	2.76	8.94	1.62	10.53
30	8.5	30	90	5.69	18.43	1.62	10.53
30	8.5	30	75	5.69	18.43	1.62	10.53
30	8.5	30	50	5.69	18.43	1.62	10.53
30	8.5	30	40	5.69	18.43	1.62	10.53
30	8.5	40	90	5.69	18.43	1.62	10.53
30	8.5	40	75	5.69	18.43	1.62	10.53
30	8.5	40	50	5.69	18.43	1.62	10.53
30	8.5	40	40	5.69	18.43	1.62	10.53
30	9.0	10	90	1.6	5.17	2.94	19.03
30	9.0	10	75	1.6	5.17	2.94	19.03
30	9.0	10	50	1.6	5.17	2.94	19.03
30	9.0	10	40	1.6	5.17	2.94	19.03
30	9.0	20	90	1.86	6.02	2.94	19.03
30	9.0	20	75	1.86	6.02	2.94	19.03
30	9.0	20	50	1.86	6.02	2.94	19.03
30	9.0	20	40	1.86	6.02	2.94	19.03
30	9.0	30	90	2.33	7.56	2.94	19.03
30	9.0	30	75	2.33	7.56	2.94	19.03
30	9.0	30	50	2.33	7.56	2.94	19.03
30	9.0	30	40	2.33	7.56	2.94	19.03
30	9.0	40	90	3.64	11.8	2.94	19.03
30	9.0	40	75	3.64	11.8	2.94	19.03
30	9.0	40	50	3.64	11.8	2.94	19.03
30	9.0	40	40	3.64	11.8	2.94	19.03
40	8.0	10	90	2.68	8.67	0.46	2.95

40	8.0	10	75	2.68	8.67	0.46	2.95
40	8.0	10	50	2.68	8.67	0.46	2.95
40	8.0	10	40	2.68	8.67	0.46	2.95
40	8.0	20	90	2.76	8.94	0.32	2.10
40	8.0	20	75	2.76	8.94	0.32	2.10
40	8.0	20	50	2.76	8.94	0.32	2.10
40	8.0	20	40	2.76	8.94	0.32	2.10
40	8.0	30	90	2.76	8.94	0.33	2.15
40	8.0	30	75	2.76	8.94	0.33	2.15
40	8.0	30	50	2.76	8.94	0.33	2.15
40	8.0	30	40	2.76	8.94	0.33	2.15
40	8.0	40	90	5.69	18.43	1.66	10.72
40	8.0	40	75	5.69	18.43	1.66	10.72
40	8.0	40	50	5.69	18.43	1.66	10.72
40	8.0	40	40	5.69	18.43	1.66	10.72
40	8.5	10	90	2.33	7.56	0.45	2.92
40	8.5	10	75	2.33	7.56	0.45	2.92
40	8.5	10	50	2.33	7.56	0.45	2.92
40	8.5	10	40	2.33	7.56	0.45	2.92
40	8.5	20	90	2.76	8.94	1.60	10.35
40	8.5	20	75	2.76	8.94	1.60	10.35
40	8.5	20	50	2.76	8.94	1.60	10.35
40	8.5	20	40	2.76	8.94	1.60	10.35
40	8.5	30	90	5.69	18.43	1.62	10.53
40	8.5	30	75	5.69	18.43	1.62	10.53
40	8.5	30	50	5.69	18.43	1.62	10.53
40	8.5	30	40	5.69	18.43	1.62	10.53
40	8.5	40	90	5.69	18.43	1.62	10.53
40	8.5	40	75	5.69	18.43	1.62	10.53
40	8.5	40	50	5.69	18.43	1.62	10.53
40	8.5	40	40	5.69	18.43	1.62	10.53
40	9.0	10	90	1.6	5.17	2.94	19.03
40	9.0	10	75	1.6	5.17	2.94	19.03
40	9.0	10	50	1.6	5.17	2.94	19.03
40	9.0	10	40	1.6	5.17	2.94	19.03
40	9.0	20	90	1.9	6.14	2.94	19.03
40	9.0	20	75	1.9	6.14	2.94	19.03
40	9.0	20	50	1.9	6.14	2.94	19.03
40	9.0	20	40	1.9	6.14	2.94	19.03

40	9.0	30	90	2.33	7.56	2.94	19.03
40	9.0	30	75	2.33	7.56	2.94	19.03
40	9.0	30	50	2.33	7.56	2.94	19.03
40	9.0	30	40	2.33	7.56	2.94	19.03
40	9.0	40	90	3.64	11.8	2.94	19.03
40	9.0	40	75	3.64	11.8	2.94	19.03
40	9.0	40	50	3.64	11.8	2.94	19.03
40	9.0	40	40	3.64	11.8	2.94	19.03

Time series for the virtual gauges in Figs. 4 and 5 are shown in Fig. S4.
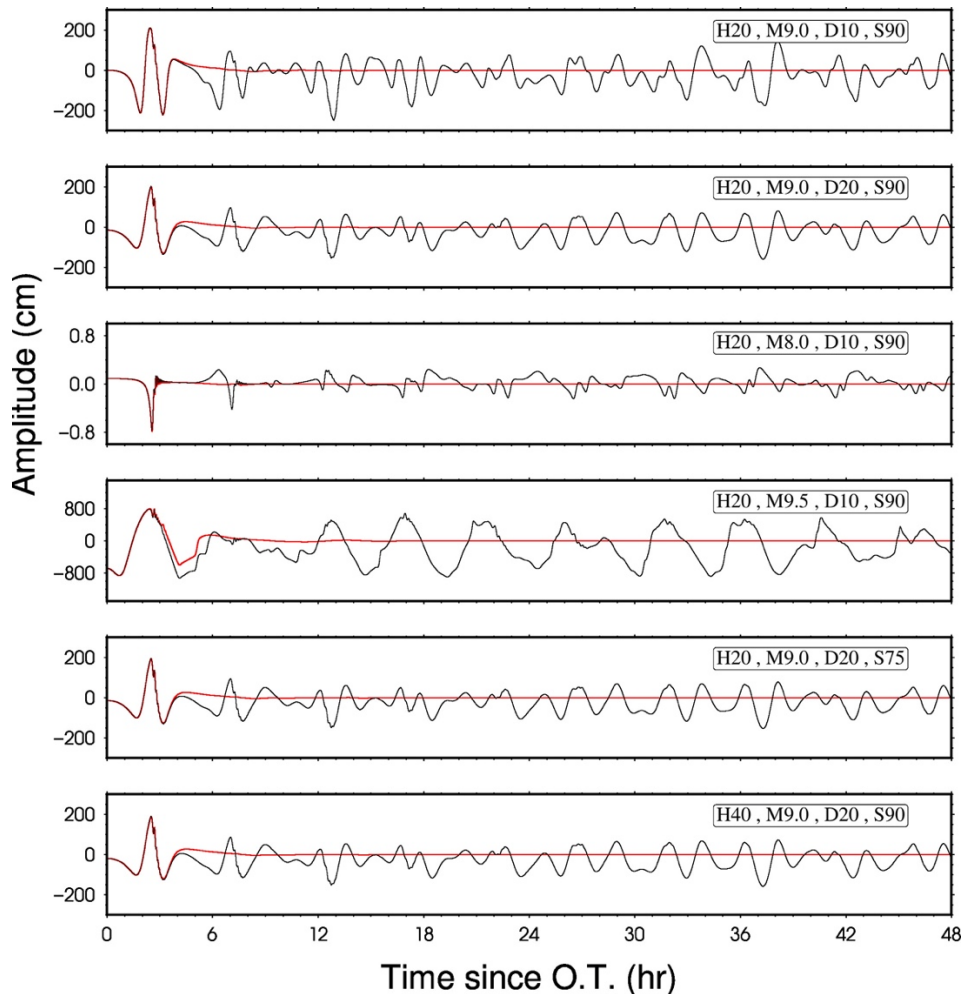
Figure S4. Time series for the virtual gauges in Figs. 4 and 5. Red and black series correspond to open and closed back-arc basins.

S4. Synthesis of Surface Wave

Given an appropriate velocity model and knowing the focal geometry of an earthquake, one can compute Raleigh wave displacements on the Earth's surface at any point relative to the epicenter. This is possible through calculating spheroidal modes of the Earth and stacking them up to any desired period to obtain appropriate excitation coefficients. The caveat here, is that calculation of higher harmonic degrees (l) becomes difficult and unstable, to some extent due to numerical issues in handling large numbers. One must also note that at such large harmonic degrees, one cannot use asymptotic solutions. However, due to the long period nature of tsunamis, it is not necessary to continue the computation of excitation coefficients up to very large values of l.

We use an approach similar to that of Saito [1967] to calculate the excitation coefficients of the first 60 spherical terms ($_0S_{60}$) for a point source translating into a period range down to 153 seconds. We then create an initial transient deformation field by accumulating the contribution of each harmonic term [Kanamori, 1970; Kanamori & Cipar, 1974; Okal, 1976].

The velocity of Rayleigh waves varies between 3.6–7.9 km/s (l=35 and l=5, respectively) as used in the modal synthesis of transient surface displacements capped at $_0S_{60}$ (for both point and finite sources). We note that in this formalism, degenerate and split modes require some extra care as they may observe different (perhaps unattainable) phase velocities (e.g., see Duan & Huang [2019]). However, we have curbed the velocity window to ensure such issues do not happen. Similarly, mode branches may pose an issue in choosing appropriate phase velocities (e.g., see pages 230-243 from Gilbert & Dziewonski, 1975).

To obtain displacement fields, we calculate synthetic seismogram of surface waves at the grid points of bathymetry data for the area of study. We then create synchronous grids for each time step by syncing the calculated synthetics. In this way, at each time step (i.e., in each "snapshot") all the grid points belong to the same moment of time. at various moments of time around the epicenter from both a point source and finite ruptures Fig. S5a shows an example of such snapshots of the Rayleigh wave amplitudes in the bathymetry grid for the CMT point source of 2011 Tohoku.

Excessive amplitudes (>40 cm) in Fig. S5a are due to the unrealistic representation of a very large rupture by a point source. In reality, interference of seismic signals imposed by a finite fault would result in smaller amplitudes. Therefore, we approximate the finite rupture as an array of point sources along the rupture, temporally offset according to their respective assigned moments [Koketsu et al, 2011] to account for rupture duration (here, set to 190 s) as shown in Fig. S5b. Our use of a 1-D array is warranted by the fact that growth in fault length reduces the width of directivity lobes [Ben-Menahem & Rosenman, 1972] which play the most important part the dominant propagation azimuth of Rayleigh waves. Supplementary videos SV1 and SV2, show computed propagation models of Ralyeigh waves for point and finite sources, respectively. The time stamps in these videos are in GMT.
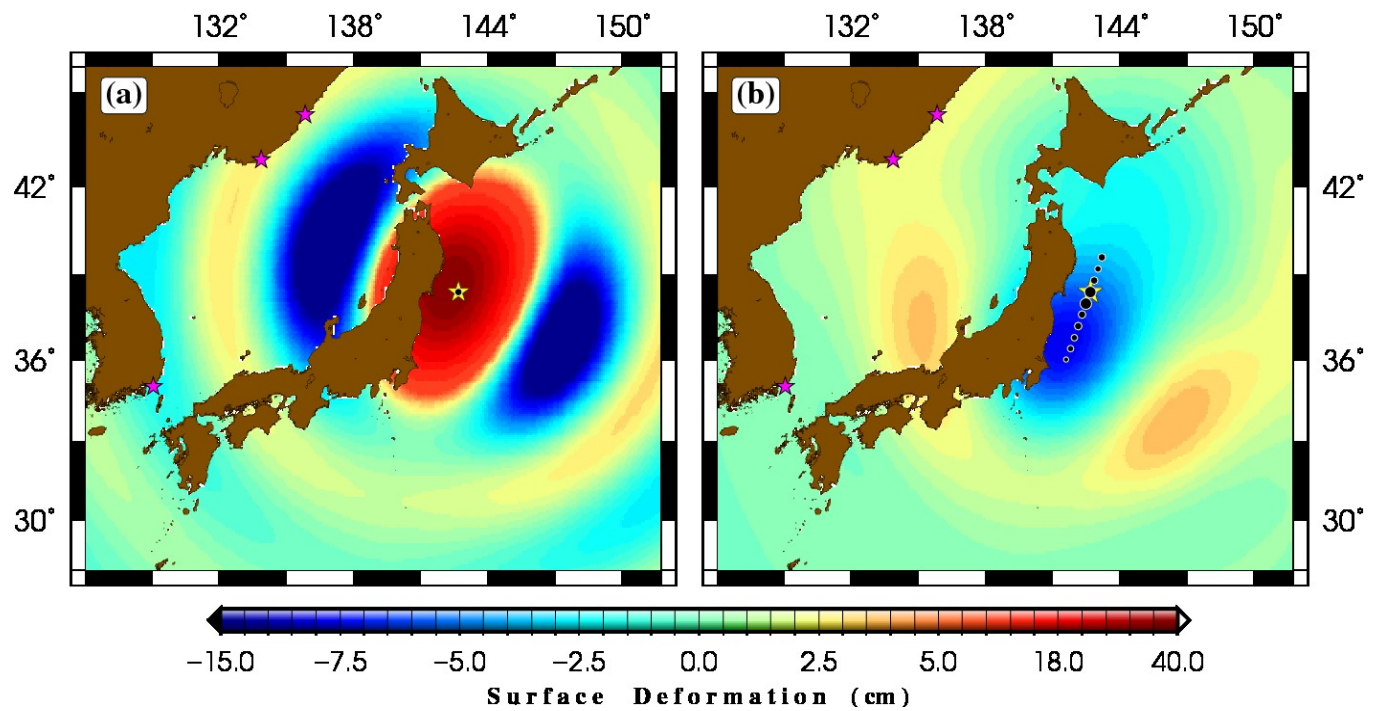
Figure S5. Deformation grid for (a) a point source at the CMT location at t=0, and (b) an array of point sources mimicking an almost bilateral rupture with assigned seismic moments [Koketsu *et al,* 2011] and "delays" relative to the origin time. The snapshot in (b) shows t=t_1 at the end of rupture dislocation (=rupture duration). Yellow stars represent rupture epicenter. The subevents in (b) are graphically scaled to reflect their respective moment. Our three gauges are shown by pink stars. Animated propagation models for (a) and (b) are available as supplementary videos SV1 and SV2.

S6. Tsunami Simulation Results of the 2011 Japan Static Source: Longer Windows

Recorded and simulated time series at the three western and five eastern sites marked in Fig. 11 are shown in Figs. S6 and S7. While there is a noticeable mismatch between the observed and simulated amplitudes (left panels of Fig. S7), as shown in the right panels of Fig. S7, there is a good match between the corresponding spectra at Okushiri and Nezugaseki. The latter means that the back-arc tsunami source and the tsunami are well-represented at these two sites in our simulations. There is, however, considerable mismatch between the two spectra in the rest of stations, at $f > 0.0006$ Hz (~1500 s). We attribute this discrepancy to the absence of higher frequency, kinematic source components (such as surface waves) and probably, insufficient bathymetric resolution. Tsunami simulation maps of the 2011 earthquake in the back-arc Sea of Japan using various components of the source are shown in Fig. S8. Only static source components are taken into account here.
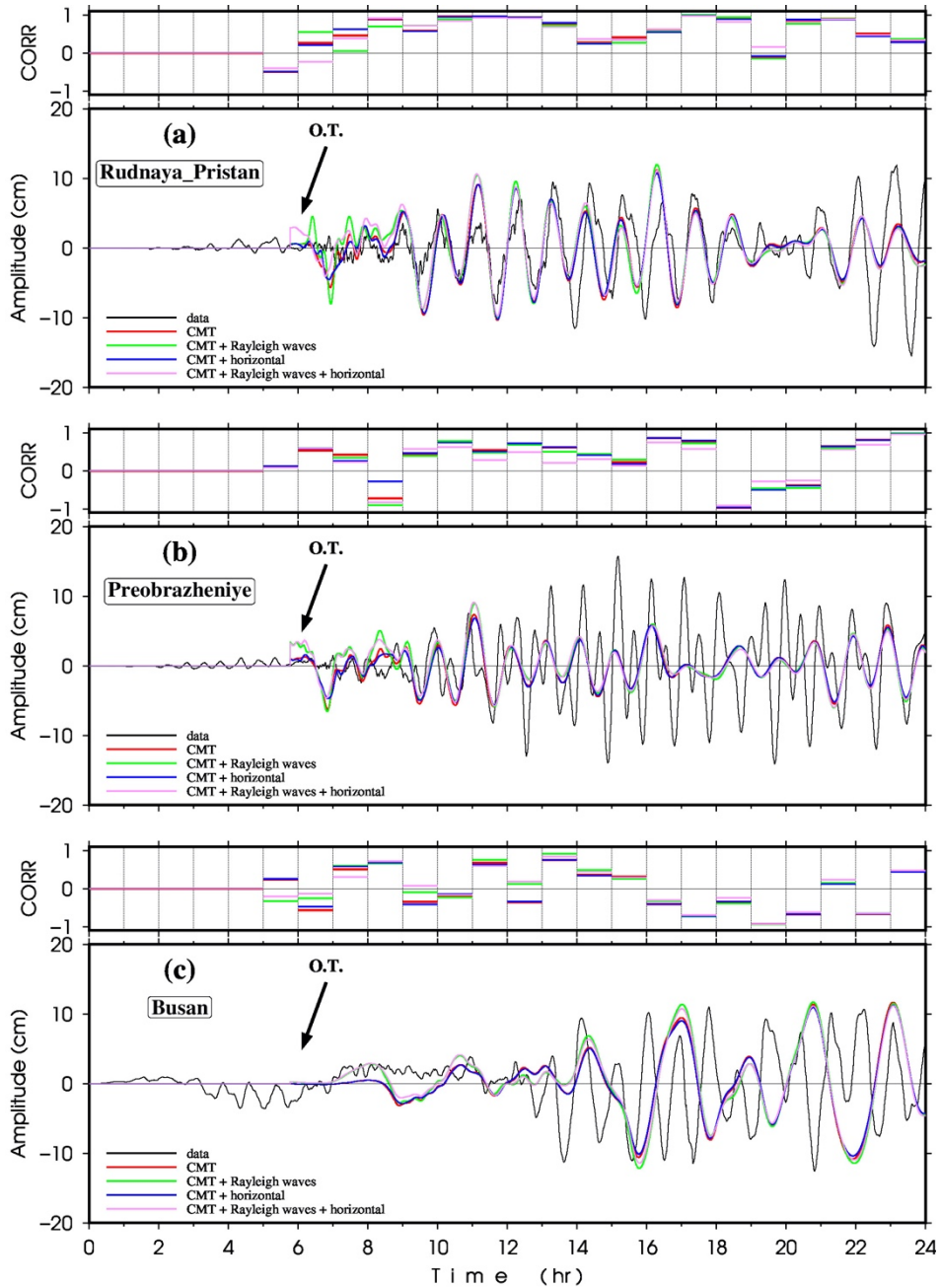
Figure S6. Tide gauge records from the 2011 Japan tsunami at three locations (a) Rudnaya Pristan, (b) Preobrazheniye, and (c) Busan, as also marked on the maps in Fig. S8(a)—(d). In each panel, recorded data is shown by a black curve. Simulation results at these locations from the scenarios in (a)—(d) are shown in different colors. Rupture origin time is marked with black arrows. Top panels in (a)—(c) show correlation coefficients of each simulated time series with the recorded data, in 1-hr intervals.
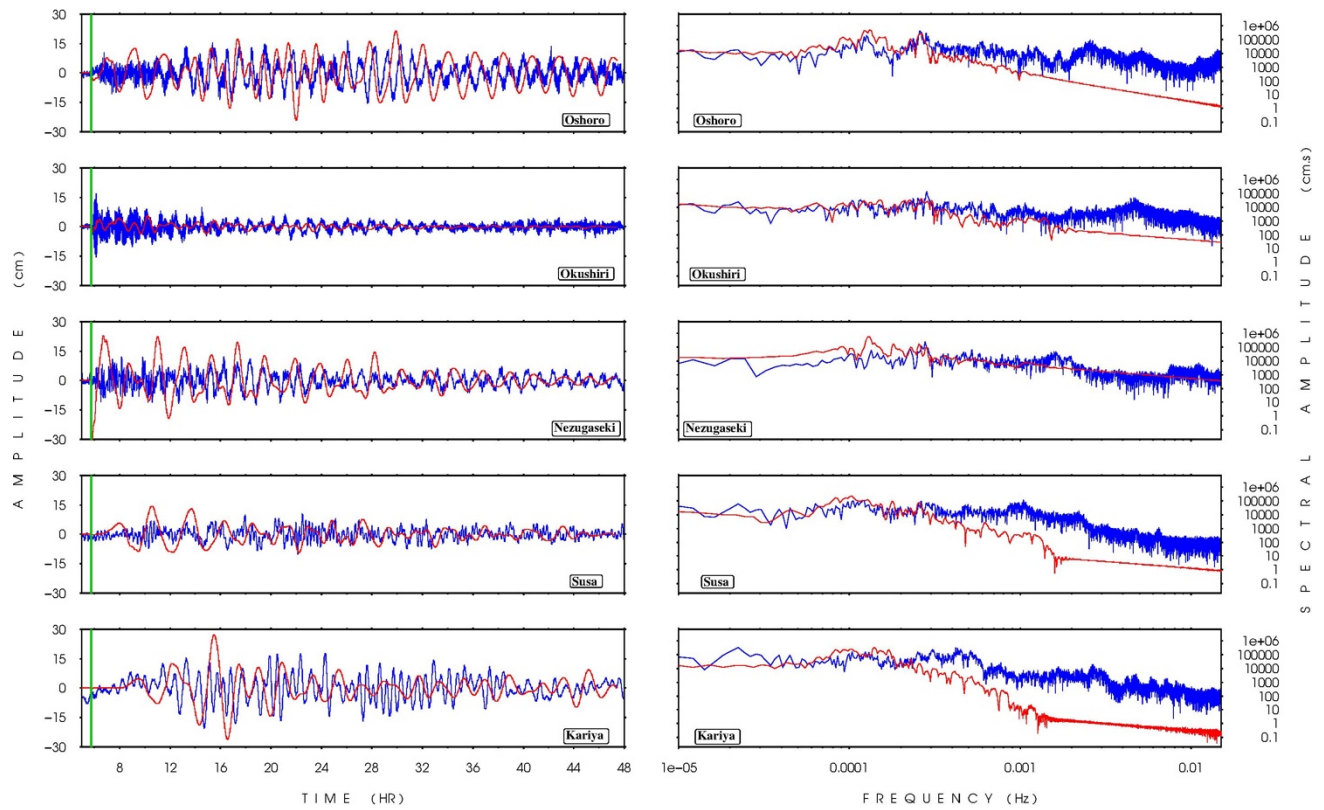
Figure S7. *(Left)* Tide gauge records (blue) and simulation results (red) at sites on the eastern coastline of the Sea of Japan. The common, vertical, green line depicts rupture origin time. Surface waves are not included here. *(Right)* Observed and simulated spectra form the corresponding panels to the left.
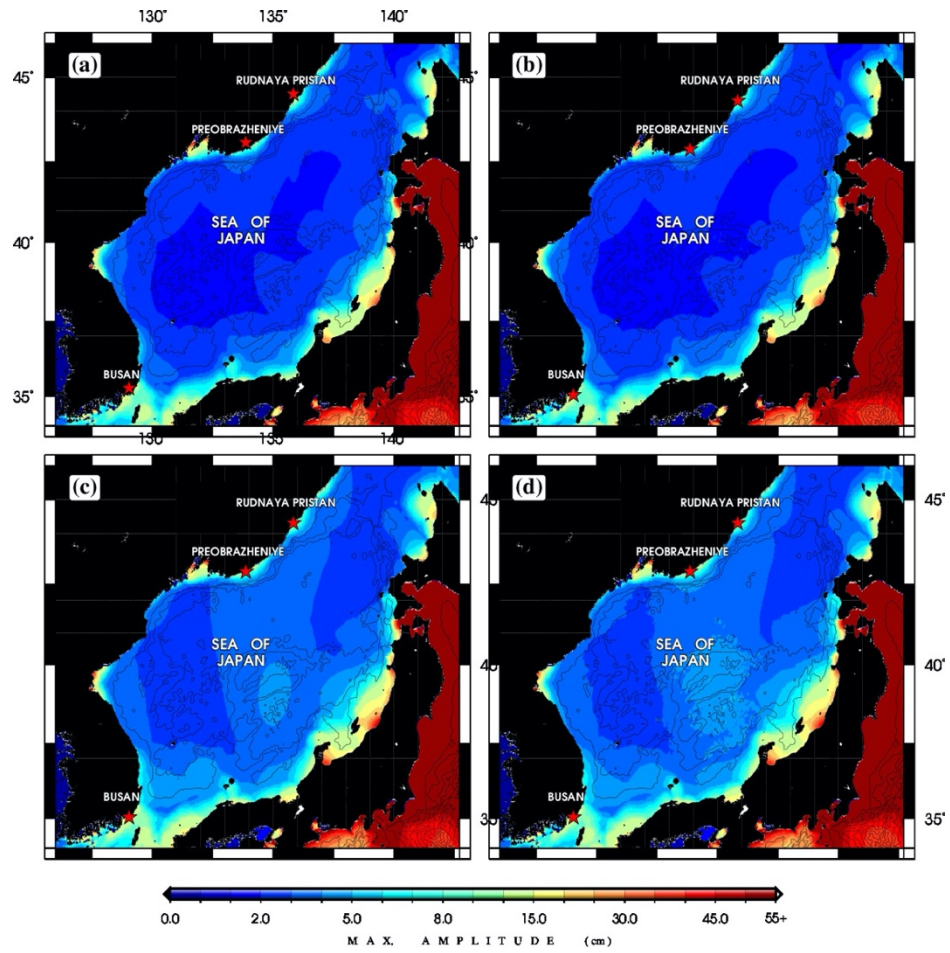
Figure S8. Simulation of the tsunami in the Sea of Japan from the 2011 Tohoku earthquake using (a) static vertical deformation from the CMT source, (b) static vertical and horizontal CMT deformation (c) static vertical CMT deformation and Rayleigh waves, and (d) combination of (a)—(c).

S6. Choice of Time Intervals for Correlation Coefficient Calculations

An important aspect comparing the time series using correlation coefficient (CC) is the choice of calculation time window (T_w) throughout the records. While the choice of time window depends on the target time resolution (i.e., minimum frequency), it is important that the comparison must be largely invariant of the choice of T_w. In the case of tide gauge records from the Sea of Japan, we can show that a good window length is ~ 30 minutes. To do so we can plot the medians of positive and negative CC values (separately) as a function of window length to find a point of change in the trend of medians. In Fig. S9, a good choice of window length is ~30 minutes beyond which there is no practical change in calculated CC values. For the changes in individual CC values at each time interval (for the station at Rudnaya Pristan) between data and simulation using four different source configurations see supplementary video SV3.
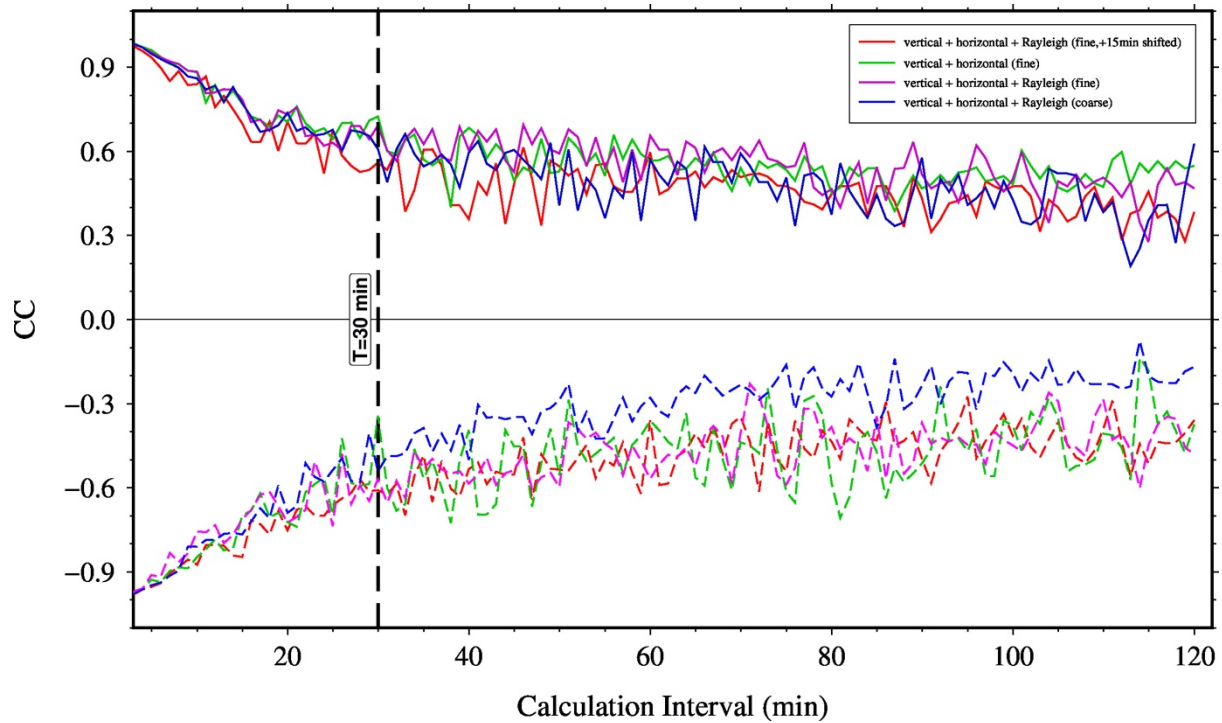
Figure S9. Median of positive and negative CC values throughout the records, calculated for various Window Lengths (1<WL<120 minutes). The change in behavior ("elbow") seems to occur around T=30 minutes.

S7. Beamforming of Tsunami in the Korea Strait

In order to investigate the roots of the complexity of the recorded signal in Busan, we calculate the time delays in first tsunami arrivals in the simulation grid with respect to Busan (Fig. S10). The simulation was carried out in the geographic window of 124°-150°E and 28°-46°N. The map in Fig. S10 (color-coded according to the calculated offsets) shows that tsunami waves from the CMT source arrive much earlier (hot colors) in the Sea of Japan to the NE that in the East China Sea to the SW (cold colors). However, in the vicinity of Busan, the arrival pattern gets more complex (note the transition of hot to cold colors). While the back-arc signal clearly arrives at Busan earlier than the fore-arc waves – which have circled Japan islands – the fore-arc signal arrives slightly less than two hours later (i.e., about three hours after the earthquake origin time).
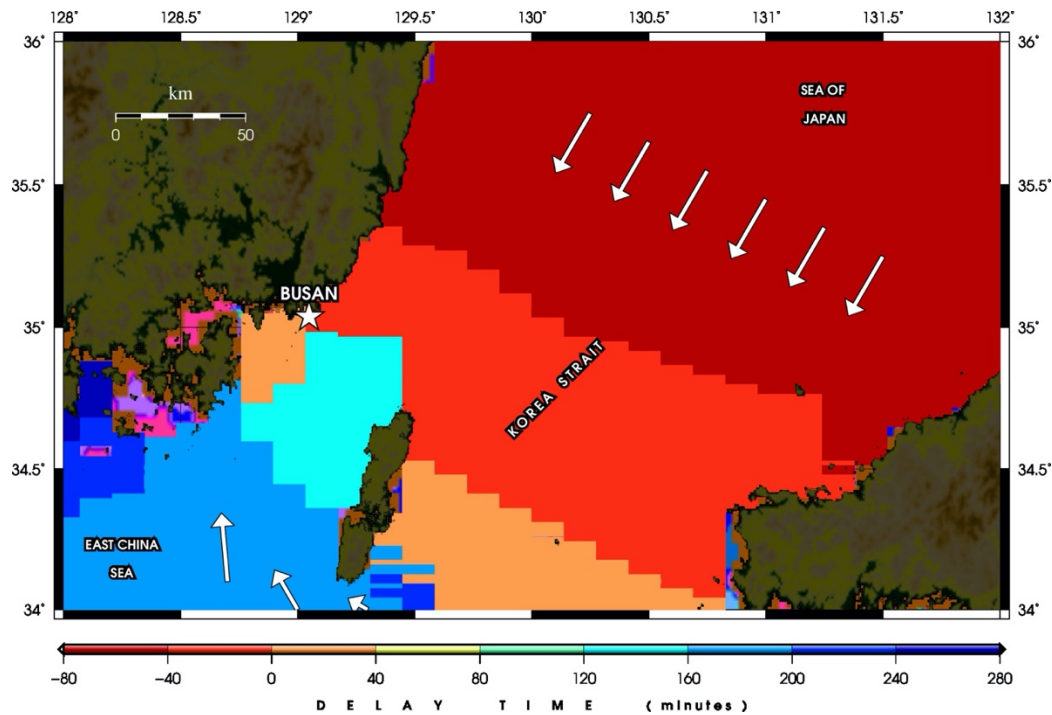
Figure S10. Relative arrivals of the simulated tsunami into the Korea Strait with respect to Busan. The map is color-coded according to delay time in minutes. Arrows show the approximate azimuths of arriving waves.

A more detailed, systematic version of the effort described above is beamforming of the tsunami in the vicinity of Busan. To this end, we find the maximum-energy "beam" in a virtual array (dots in Fig. S11) designed in our numerical simulation of the tsunami. The maximum-energy beam corresponds to the azimuth of coherent incoming waves, i.e., when the recorded waveforms from all stations are in sync. We adopt a simple, 2-D, time-domain beamforming approach [e.g., Rost & Thomas, 2002] by setting the incidence angle to $\theta = 90°$ (i.e., horizontal propagation) and dropping the altitude term (gauges are placed on the global geoid) and assuming a constant velocity under the virtual array. The latter is chosen as the average group velocity of the tsunami at the location of each virtual station, calculated from shallow water approximation. By using the long-period part of energy and placing stations away from the shorelines, we consider "planar" wavefronts, hence satisfying the constraints of our simplified beamforming.

Fig. S11 shows examples of beamforming results for various time windows in our simulations (a complete set of the outputs throughout the 48 hr simulation is available as supplementary video SV4). The flip-flops in the dominant azimuth of the array beam shows significant changes in the propagation direction of incoming waves as well as the influence of large-scale reflections. The initial beam azimuth of ~300º at earthquake origin time (~6000 s before first significant arrival) which lasts for only a few minutes corresponds to the small arrivals from the west, i.e., the direction of small positive deformation next to node. After a series of fast changes in the dominant azimuth, lasting for about 2 hours, between first very small waves and their reflections, the first significant appearance of the tsunami arrives from NE, i.e., the Sea of Japan. About ~3 hours later, the dominant azimuth starts to constantly vary between

~90º and ~270º. This time coincides with the arrival of the secondary wavefronts from the Pacific.

  This simple analysis explains the complexity of the tsunami waveform recorded at Busan during the 2011 Japan tsunami. This complexity results in the mismatch between the observed data and our simple model.
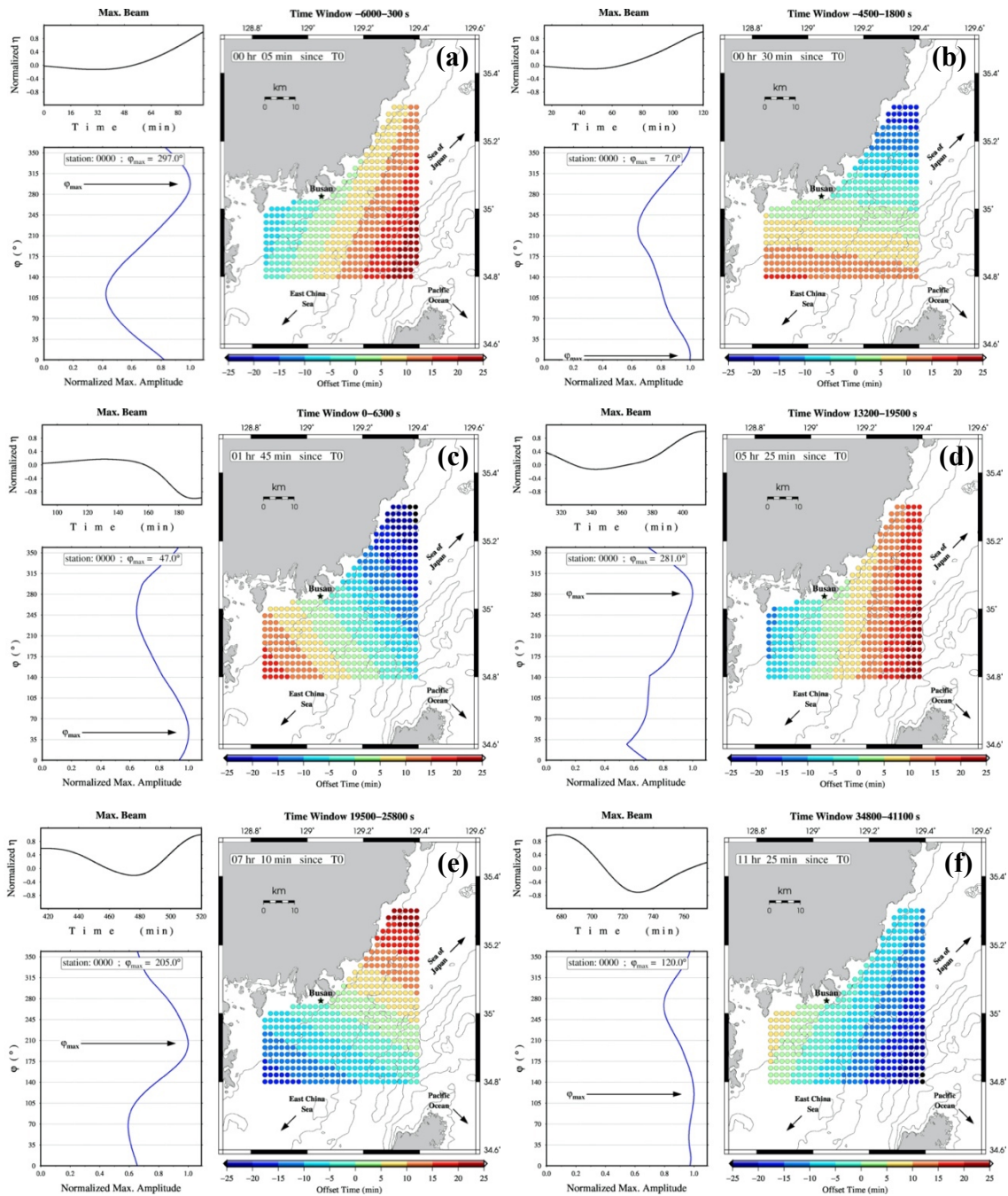
Figure S11. (a—f) Examples of beamforming results for tsunami arrivals in the Busan region over 01hr:45min time intervals; times are relative to T_0, i.e., the first noticeable (>1mm) arrival [this is a generic threshold, approximately equal to the amplitude of smallest detected tsunamis from large deep earthquakes; see Okal, 2017]. In each of the six shown time intervals, the top left panel shows the maximum-energy array beam, the bottom left panel shows the distribution of maximum beam amplitude over azimuth with the black arrow marking the azimuth of maximum energy, and the right panel shows the map view of calculated delay times with respect to Busan.

S8. Ray-tracing of coastal sources

Propagation of tsunami waves can be approximated using ray-tracing techniques [Woods & Okal,1987; Satake, 1988]. These methods are based on the solution of the 2-D Eikonal equations on a heterogeneous sphere [e.g., Jobert & Jobert, 1983] using a field of variable propagation velocities in the shallow-water approximation. The resulting equations can be numerically solved for a given velocity field in the form of a regular grid. While these methods consider only point sources, hence ignoring source structure, they are valuable in identifying the general trends of propagation.

In a simplistic model of the back-arc 2011 tsunami, one may assume the Japanese coastlines to be secondary sources of energy in the Sea of Japan. Ray-tracing for an example of such sources placed at the location of largest back-arc deformation is shown in Fig. S12. An important feature of Fig. S12 is the complicated wavefront in the southern and eastern Sea of Japan due to the entrapment of high-frequency energetics in the complex bathymetry. This leads to the apparent better match between our simulations and the observed data in the north (compared to Busan), for the high-frequency part of the time-series.
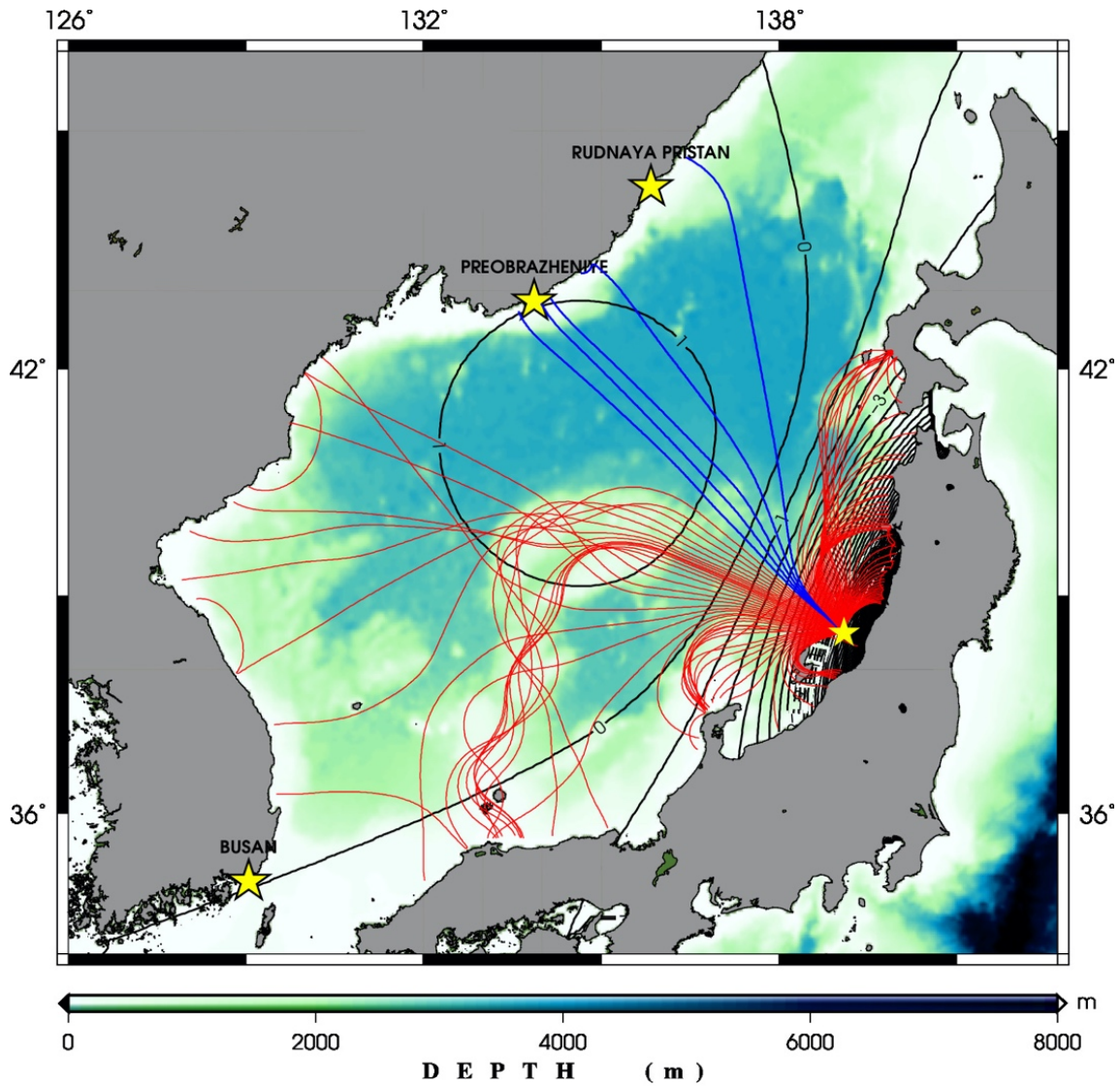
Figure S12. Ray-tracing of a secondary point source (yellow star) in the Sea of Japan shown on bathymetry as background (color-coded according to the scale bar). The rays leave the point source at 2° increments and those arriving at the northern sites are highlighted in blue. Back-arc deformation is shown with black contours.

S9. Spectral Content of Tide Gauge Records from Station on the West of the Ses of Japan.Coast

Comparison of the spectral content of the tide gauge data from western stations (Fig. S13) reveals higher frequencies in early hours of back-arc propagation only at Rudnaya Pristan (Fig. S13a) which is located at simpler bathymetry.
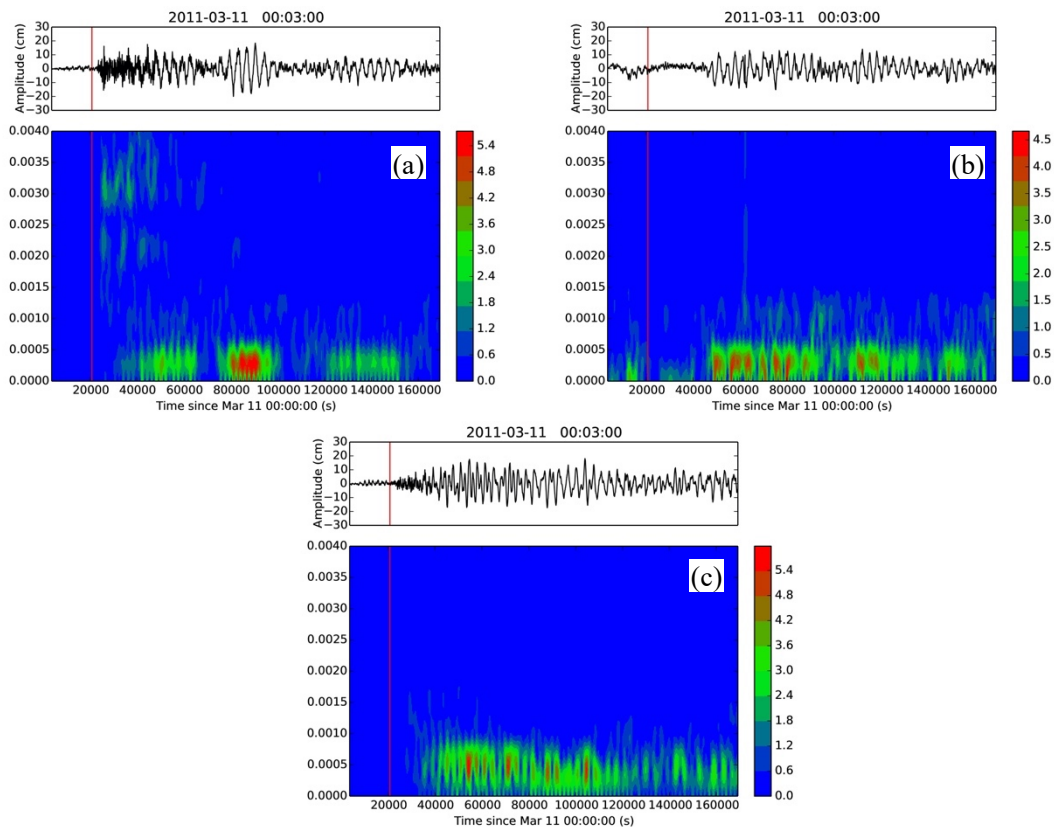

Figure S13. Spectrograms of tide gauge data from **(a)** Rudnaya Pristan, **(b)** Preobrazheniye, and **(c)** Busan. Vertical red lines show earthquake origin time.

S10. Japan Trench Source Scenarios

Table S2 lists the historical sources in the Japan Trench used in constructing the rupture scenarios in this study.

Table S2. Source parameters of the 1936–1978 sequence. The 1936 mechanism is replaced with that of the 16 Aug. 2005 event for the sake of higher quality data.

No.	Date	Lon.	Lat.	Depth (km)	M_0 (dyn-cm)	φ	δ	λ	Source
1	27 Jul. 1937	142.00	38.05	30	7.1	200	45	90	Umino (2006)
2	23 May 1938	141.34	36.58	40	7.4	200	10	100	Abe (1977)
3	05 Nov. 1938	141.71	36.97	30	7.7	200	10	95	Abe (1977)
4	05 Nov. 1938	141.75	37.24	45	7.8	200	10	108	Abe (1977)
5	06 Nov. 1938	142.18	37.33	17	7.7	190	80	90	Abe (1977)
6	06 Nov. 1938	142.19	36.91	33	7.1	190	80	90	Abe (1977)
7	12 Jun. 1978	142.22	38.15	28	7.4	190	20	76	Seno *et al* (1980)
8	16 Aug. 2005	142.04	38.28	36	7.2	194	16	81	CMT
Total	-	141.80	38.20	20	8.8	195	31	86	*calculated*

S11. Nankai Trough Tsunami Scenarios

Table S3 lists source properties of the four Nankai Trough rupture scenarios.

Table S3. Source parameters of the Nankai Trough scenarios. Blocks are adopted from Furumura *et al* (2011).

Model	Blocks in the Rupture					Epicenter		Depth (km)	Length (km)	Width (km)	Slip (m)	M_0 $(10^{28}$ dyn-cm)	φ	δ	λ
	N_5	N_4	N_3	N_2	N_1	Lat.	Lon.								
I		▓	▓			134.60	32.55	8.9	280	110	7.4	10	250	10	113
II		▓	▓	▓		135.48	32.83	7.3	485	110	7.3	20	250	10	113
III		▓	▓	▓	▓	136.24	32.27	7.1	605	95	6.9	20	240	12	103
IV	▓	▓	▓	▓	▓	135.54	33.04	7.7	685	90	7.3	20	240	12	106

S12. Effect of Near-Field Back-arc Deformation

We can compare the contribution of different segment of the back-arc deformation field to the excitation of back-arc tsunami by dividing the field into individual deformation blocks and simulating the tsunami from various combination of these "subevents". In Fig. S14, tsunami propagation maps from a set of small (i.e., short period), large amplitude (-30 cm) source blocks along the western coast of Japan (Fig. S14a), and a single large (i.e., long period), small amplitude (2 cm) source block in central Sea of Japan (Fig. S14b) are compared. These blocks and their amplitudes are designed to match the original deformation field from the CMT solution for the 2011 Tohoku rupture.

The combined set of the former group constitutes the near-field back-arc deformation whereas the latter can be thought as the far-field component. Figs. S14c and S14d compare the recorded time series at Rudnaya Pristan (green) to the simulated time series (red) from the two scenarios. We note that while the near-field sources succeed in matching amplitudes and better match the long-period section of the records, the far-field scenario provides a better fit to the high frequency part of the record, i.e., the first few hours after origin time.
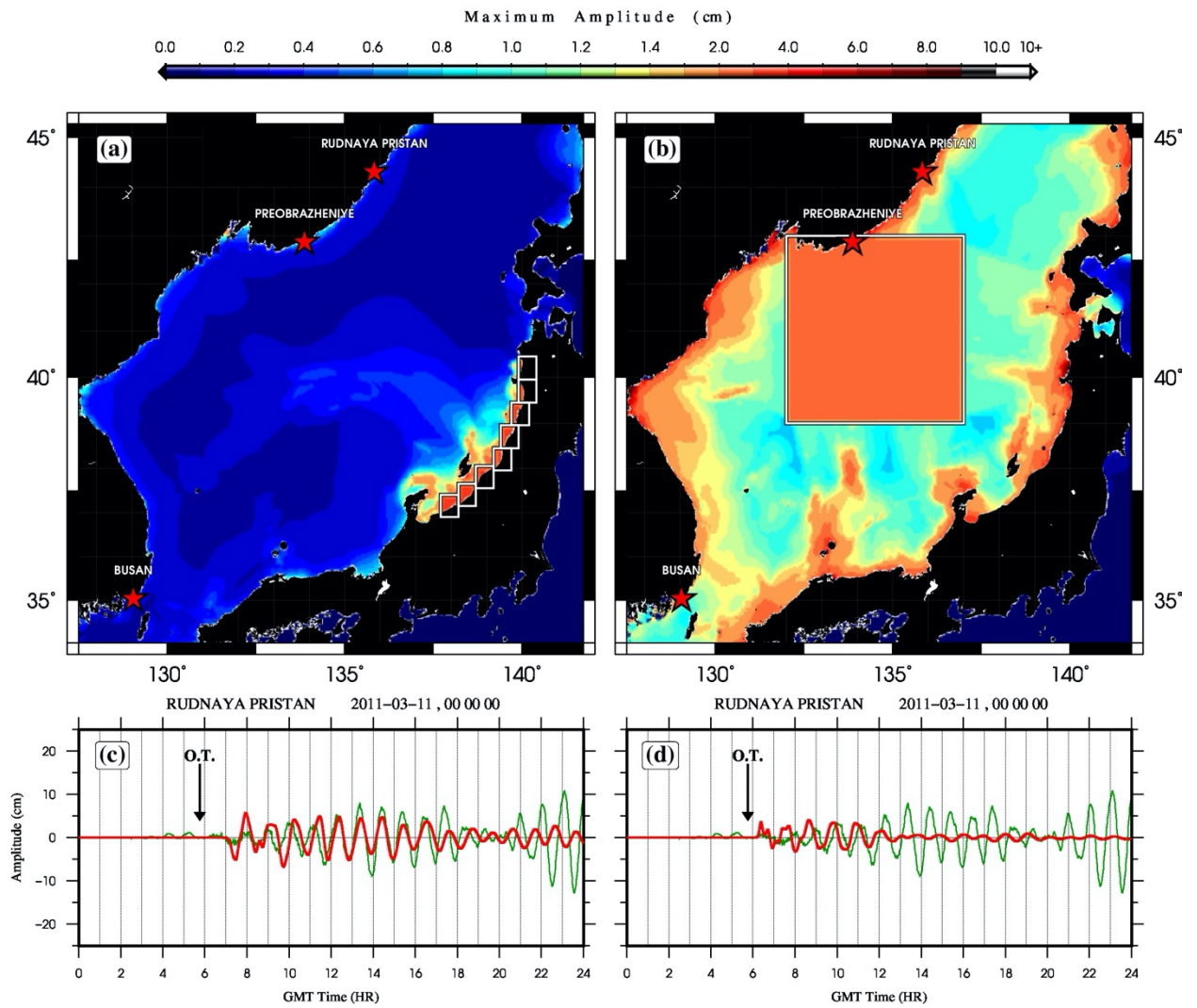
Figure S14. Comparison of the contribution of **(a)** near- and **(b)** far-field deformations to the time series (**(c)** and **(d)**) recorded at Rudnaya Pristan. Vertical, black arrows show earthquake origin time.

S13. Simulation of 2004 Sumatra tsunami

A good example in the excitation of back-arc tsunamis in other regions is Sumatra.

Simulation of the tsunami from 2004 M_w=9.3 rupture shows that although the large trench-to-

coast distance in southern Sumatra prevents the formation of back-arc waves, in the north where

the arc turns into a narrow island chain (Andaman & Nicobar), a tsunami indeed appears in the

Gulf of Thailand with no direct connection to the fore-arc (see Fig. S15). Although the

centimetric amplitude of the tsunami in the Gulf of Thailand cannot be confirmed due to the lack

of appropriate gauge data, this sets an interesting example of back-arc tsunamis with coastlines

more than 800 km away from the trench. We use the composite source from Salaree & Okal

(2020) as the initial condition in the simulation of 2004 tsunami. The simulation result is shown
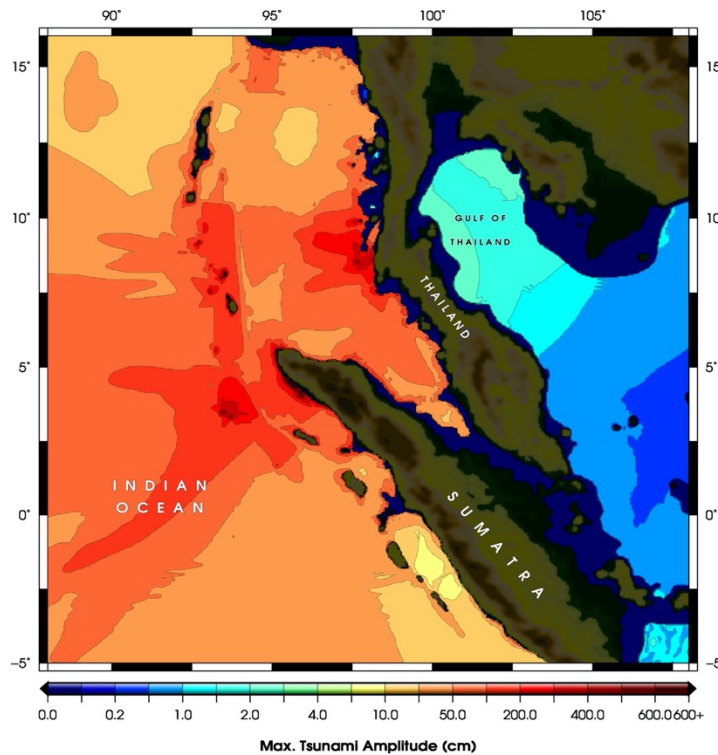
in Fig. S15.

Figure S15. Simulation of the 2004 Sumatra tsunami.

References

- Abe, K., 1977. Tectonic implications of the large Shioya-Oki earthquakes of 1938. *Tectonophysics*, **41**(4), pp.269-289.

- Ben-Menahem, A. and Rosenman, M., 1972. Amplitude patterns of tsunami waves from submarine earthquakes. *Journal of Geophysical Research*, **77**(17), pp.3097-3128.

- Duan, P. and Huang, C., 2019. Application of normal Morlet wavelet transform method to the damped harmonic analysis: On the isolation of the seismic normal modes ($_0S_0$ and $_0S_5$) in time domain. *Physics of the Earth and Planetary Interiors*, 288, pp.26-36.

- Furumura, T., Imai, K. and Maeda, T., 2011. A revised tsunami source model for the 1707 Hoei earthquake and simulation of tsunami inundation of Ryujin Lake, Kyushu, Japan. *Journal of Geophysical Research: Solid Earth*, **116**(B2).

- Gilbert, F. and Dziewonski, A.M., 1975. An application of normal mode theory to the retrieval of structural parameters and source mechanisms from seismic spectra. *Philosophical Transactions of the Royal Society of London*. **in:** Series A, Mathematical and Physical Sciences, 278(1280), pp.187-269.

- Kanamori, H. & Cipar, J. J., 1974. Focal process of the great Chilean earth- quake May 22, 1960, *Physics of the Earth and Planetary Interiors*, **9**(2), 128–136.

- Kanamori, H., 1970. Synthesis of the long-period surface waves and its application to earthquake source studies–Kurile Islands earthquake of October 13, 1963, *Journal of Geophysical Research,* **75**(26), 5011–5027.

- Kian, R., 2015. Tsunami induced wave and current amplification and sedimentation in closed basins (Doctoral dissertation, *Ph. D. Dissertation*, Middle East Technical University, Ankara, Turkey), 189 pp.

- Koketsu, K., Yokota, Y., Nishimura, N., Yagi, Y., Miyazaki, S.I., Satake, K., Fujii, Y., Miyake, H., Sakai, S.I., Yamanaka, Y. and Okada, T., 2011. A unified source model for the 2011 Tohoku earthquake. *Earth and Planetary Science Letters*, **310**(3-4), pp.480-487.

- Mai, P.M. and Thingbaijam, K.K.S., 2014. SRCMOD: An online database of finite-fault rupture models. *Seismological Research Letters*, **85**(6), pp.1348-1357.

- Okal, E.A., 1976. A surface-wave investigation of the rupture mechanism of the Gobi-Altai (December 4, 1957) earthquake. *Physics of the Earth and Planetary Interiors*, **12**(4), pp.319-328.

- Okal, E.A., 2017. The excitation of tsunamis by deep earthquakes. *Geophysical Journal International*, **209**(1), pp.234-249.

- Rost, S. and Thomas, C., 2002. Array seismology: Methods and applications. *Reviews of geophysics*, **40**(3), pp.2-1.

- Saito, M., 1967. Excitation of free oscillations and surface waves by a point source in a vertically heterogeneous earth. *Journal of Geophysical Research*, **72**(14), pp.3689-3699.

- Salaree, A. and Okal, E.A., 2020. Tsunami simulations along the Eastern African coast from mega-earthquake sources in the Indian Ocean. *Arabian Journal of Geosciences*, **13**(20), pp.1-13.

- Satake, K., 1988. Effects of bathymetry on tsunami propagation: Application of ray tracing to tsunamis. *Pure and Applied Geophysics*, **126**(1), pp.27-36.

- Seno, T., Shimazaki, K., Somerville, P., Sudo, K. and Eguchi, T., 1980. Rupture process of the Miyagi-Oki, Japan, earthquake of June 12, 1978. *Physics of the Earth and Planetary Interiors,* **23**(1), pp.39-61.

- Titov, V.V., Mofjeld, H.O., González, F.I. and Newman, J.C., 1999. Offshore forecasting of Hawaiian tsunamis generated in Alaskan-Aleutian subduction zone. *NOAA Technical Memorandum ERL PMEL*, **114**, p.22.

- Umino, N., Kono, T., Okada, T., Nakajima, J., Matsuzawa, T., Uchida, N., Hasegawa, A., Tamura, Y. and Aoki, G., 2006. Revisiting the three M-7 Miyagi-oki earthquakes in the 1930s: possible seismogenic slip on asperities that were re-ruptured during the 1978 M= 7.4 Miyagi-oki earthquake. *Earth, planets and space*, **58**(12), pp.1587-1592.

- Woods, M.T. and Okal, E.A., 1987. Effect of variable bathymetry on the amplitude of teleseismic tsunamis: A ray-tracing experiment. *Geophysical Research Letters*, **14**(7), pp.765-768.